Exceptional-Point-Based Optical Amplifiers

Q. Zhong[1], S.K. Ozdemir,[2] A. Eisfeld,[3] A. Metelmann,[4,*] and R. El-Ganainy[1,5,†]

[1]*Department of Physics and Henes Center for Quantum Phenomena, Michigan Technological University, Houghton, Michigan 49931, USA*

[2]*Department of Engineering Science and Mechanics, and Materials Research Institute, The Pennsylvania State University, University Park, Pennsylvania 16802, USA*

[3]*Max Planck Institute for the Physics of Complex Systems, Nöthnitzer Strasse 38, 01187 Dresden, Germany*

[4]*Dahlem Center for Complex Quantum Systems and Fachbereich Physik, Freie Universität Berlin, 14195 Berlin, Germany*

[5]*Department of Electrical and Computer Engineering, Michigan Technological University, Houghton, Michigan 49931, USA*

The gain-bandwidth product is a fundamental figure of merit that restricts the operation of optical amplifiers. Here, we introduce a design paradigm based on exceptional points, which relaxes this limitation and allows for the building of a new generation of optical amplifiers that exhibits a better gain-bandwidth scaling. Additionally, our results can be extended to other physical systems such as acoustics and microwaves.

I. INTRODUCTION

The quest for new photonic devices and functionalities is currently pushing the limit for novel design paradigms and material platforms. One of the most fundamental processes in optical science and engineering is signal amplification. Current amplification mechanisms include incoherent pumping (atomic or band inversion followed by stimulated emission) or coherent pumping (such as in nonlinear wave-mixing processes). Based on their geometry, optical amplifiers (OAs) [1,2] can be classified into traveling-wave [3] or standing-wave [4] devices. The former offers a larger bandwidth of operation at the expense of attainable gain and footprint (a few millimeters in length). On the other hand, the latter can have larger gain due to the power recycling in the resonator, which allows for a much smaller device size, suitable for large-scale integration. However, the same resonant condition leads to a very narrow bandwidth. This fundamental limitation pertinent to cavity-based optical amplifiers (and generally also to electronic and microwave amplifiers) is known as the gain-bandwidth product and is often expressed as [5]: $\chi = \sqrt{G}B = $ constant, where G is the maximum gain and B is the bandwidth [which is usually defined as the full width at half maximum (FWHM) of the power-gain curve—here, we adopt this definition]. Relaxation of this constraint beyond its standard scaling will enable a

new level of integration for high-performance photonic circuits. Previous studies have demonstrated noise-free phase-sensitive amplification that is not limited by any fundamental gain-bandwidth constraint in parametrically driven coupled-mode systems [6–10]. There, one combines parametric amplification with frequency-conversion processes, which effectively removes the instability introduced by the amplification process. Such multitone setups require well-controlled pump amplitudes and demand strong external driving, which can be rather challenging. Thus it is desirable to develop simpler designs that exhibit improved gain-bandwidth behavior.

Here, we introduce an OA scheme based on optical resonators operating at exceptional points (EPs)—special types of singularity that arise in systems described by non-Hermitian Hamiltonians when two or more eigenvalues and the corresponding eigenstates of the Hamiltonian coalesce [11–15]. We show that the gain-bandwidth product of the proposed device scales differently from that of standard resonator-based amplifiers and leads to improved performance without requiring any additional control tones. These predictions are confirmed by performing full-wave finite-difference time-domain (FDTD) analysis using realistic microring-resonator geometries and material parameters.

To this end, we consider the structure shown in Fig. 1. This device consists of a microring resonator coupled to two identical waveguides, one of which is terminated by a mirror, while the other is used as an input and output port. Optical gain is applied to the ring where the amplification

---

process takes place. In the absence of the mirror, the system has two orthogonal eigenmodes, clockwise (CW) and counterclockwise (CCW), with identical resonant frequencies ω_0. This type of spectral degeneracy with coalesced eigenvalues but orthogonal eigenmodes is referred to as a diabolic point (DP). Thus our device without the mirror operates at a DP. Under this condition and by using temporal coupled-mode theory (TCMT) [16,17], we find the scattering coefficient between the input (s_1) and output (s_3) ports as follows [16]:

$$s_{31} \equiv \frac{s_3}{s_1} = \frac{-2\gamma}{i(\omega - \omega_0) + 2\gamma + \alpha - g}, \quad (1)$$

where α is the decay rate due to loss (radiation and material losses, excluding those caused by coupling to the waveguides), γ is the loss rate due to coupling to each of the two waveguides, g is the applied gain rate, and ω is the angular frequency of the input signal. From Eq. (1), we obtain the maximum power amplification at resonance as $G_{DP} \equiv |s_{31}(\omega_0)|^2 = 4\gamma^2/(2\gamma + \alpha - g)^2$ and the bandwidth (in terms of angular frequency) as $B_{DP} = 2(2\gamma + \alpha - g)$. Substituting $2\gamma + \alpha - g = 2\gamma (G_{DP})^{-1/2}$ into the expression for B_{DP}, we obtain the following relation:

$$\chi_{DP} \equiv \sqrt{G_{DP}} B_{DP} = 4\gamma, \quad (2)$$

which is defined as the gain-bandwidth product for an amplifier with a first-order pole and is consistent with the discussion in Ref. [5]. It is clear that, for this amplifier, the gain-bandwidth product is constant and is limited by the waveguide-resonator coupling rate γ. The subscript DP here emphasizes that these quantities are obtained for an optical amplifier operating at a DP.

II. AMPLIFICATION AT EXCEPTIONAL POINTS

We now investigate the behavior of the same system in the presence of the mirror. We first do so by using TCMT [18]:

$$\frac{da_{cw}}{dt} = [i(\omega_0 - \omega) - 2\gamma - \alpha + g]a_{cw} + \sqrt{2\gamma}s_1,$$

$$\frac{da_{ccw}}{dt} = [i(\omega_0 - \omega) - 2\gamma - \alpha + g]a_{ccw} + \sqrt{2\gamma}s_3 re^{i\phi},$$

$$s_3 = -\sqrt{2\gamma}a_{cw},$$

$$s_5 = -\sqrt{2\gamma}a_{ccw},$$

$$(3)$$

where we consider s_5 to be the output port, a_{cw} and a_{ccw} are the amplitudes of the resonator mode in the CW and CCW direction, respectively, r is the magnitude of the field-reflection coefficient of the mirror, and $\exp(i\phi)$ is an additional phase due to reflection and propagation
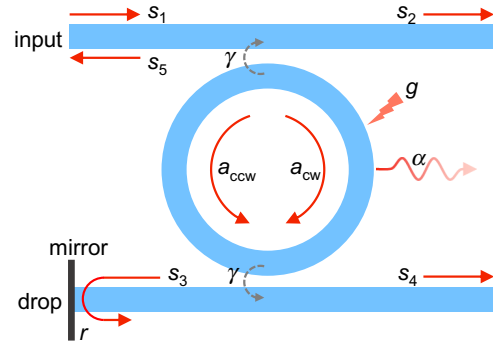

FIG. 1. The schematics of the proposed optical amplifier (OA) based on a microring resonator working at an exceptional point (EP). The input s_1 couples into the microring resonator (coupling rate γ) and is amplified by the gain g. The clockwise mode a_{cw} couples into the counterclockwise mode a_{ccw}, while the opposite is not true because of the mirror at the drop port. The output s_5 is amplified in this process. Here, r is the magnitude of the field-reflection coefficient of the mirror and α is the decay rate due to radiation and material losses.

in the waveguide. In the absence of any input signal, the above system is described by the following effective coupled-mode equations:

$$i\frac{d}{dt}\begin{bmatrix} a_{cw} \\ a_{ccw} \end{bmatrix} = H \begin{bmatrix} a_{cw} \\ a_{ccw} \end{bmatrix}, \quad H = \begin{bmatrix} \Omega & 0 \\ -2i\gamma re^{i\phi} & \Omega \end{bmatrix}, \quad (4)$$

where $\Omega = \omega - \omega_0 - i(2\gamma + \alpha - g)$. Interestingly, H is a nondiagonalizable Jordan matrix that features a chiral EP [18], which has been previously implemented by controllably placing scatterers within the mode volume of a resonator [19–21]. We emphasize that the unidirectional coupling in the Hamiltonian H does not break the reciprocity between the input and output ports of the waveguide [21,22].

Under external driving from port s_1, the scattering coefficient between the input and output ports is as follows:

$$s_{51} \equiv \frac{s_5}{s_1} = \frac{4re^{i\phi}\gamma^2}{[i(\omega - \omega_0) + 2\gamma + \alpha - g]^2}. \quad (5)$$

This solution is only valid below the lasing threshold $g = 2\gamma + \alpha$. Importantly, the scattering coefficient s_{51} exhibits a double pole as compared to the single pole in Eq. (1). As we will see shortly, this will have drastic consequences. Under these conditions, the maximum value of the amplification is $G_{EP} \equiv |s_{51}(\omega_0)|^2 = 16r^2\gamma^4/(2\gamma + \alpha - g)^4$. On the other hand, the bandwidth obtained from Eq. (5) by setting $|s_{51}(\omega)|^2 = G_{EP}/2$ is given by $B_{EP} = 2F(2\gamma + \alpha - g)$ with $F = \sqrt{\sqrt{2} - 1} \approx 0.64$. The subscript EP here emphasizes that these quantities are obtained when the system operates at a chiral EP. When comparing these results with those obtained for the DP-based amplifiers, we find that the
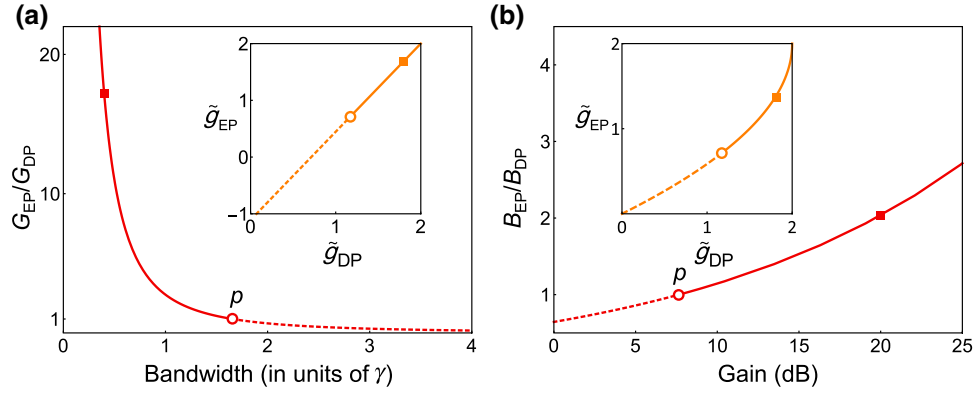
FIG. 2. (a) Amplification enhancement for an EP-based OA (as compared with the standard DP-based OA) as a function of their identical bandwidths as measured in units of γ. (b) The same as in (a) but for bandwidth enhancement as a function of the identical amplification. The insets in (a) and (b) show the relations between the material gain values that are necessary to achieve identical bandwidths or identical amplifications, respectively (see the text). Finally, the squares indicate the parameters used in the full-wave simulation (see Sec. III). These plots are obtained for $r = 1$.

bandwidth in the current scenario is reduced by a factor of F, while the gain is enhanced according to the quadratic relation $G_{EP} = r^2 G_{DP}^2$. Following the same process as in the derivation of Eq. (2), we substitute $2\gamma + \alpha - g = 2\gamma r^{1/2}(G_{EP})^{-1/4}$ obtained from the above expression for G_{EP} into the expression for B_{EP} and obtain the following relation:

$$\chi_{EP} \equiv G_{EP}^{1/4} B_{EP} = 4\gamma F \sqrt{r}. \tag{6}$$

In the spirit of Eq. (2), we define the expression in Eq. (6) as the gain-bandwidth product for an amplifier operating at an EP. Clearly, χ_{EP} defined in Eq. (6) is constant and limited by the device parameters γ (as is the case for χ_{DP}) and the reflectivity r of the mirror. We note here that the proposed device operating at an EP corresponds to an amplifier with a second-order pole. Equation (6) is one of the central results of this work. It shows that the gain-bandwidth product for the EP regime scales differently than for the case of a DP. As we will demonstrate below, this provides superior performance over the standard amplifier operating at a DP.

We first consider the case when the two amplifiers based on an EP and a DP, respectively, have the same bandwidth. This occurs for different levels of pumping related by $\tilde{g}_{EP} = F^{-1}\tilde{g}_{DP} + 2(1 - F^{-1})$, where $\tilde{g} = (g - \alpha)/\gamma$, and α, γ are identical for both amplifiers but g is different. Under these conditions, the amplification-enhancement factor η_G is:

$$\eta_G \equiv \frac{G_{EP}}{G_{DP}}\Big|_{B_{EP}=B_{DP}} = \frac{4r^2 F^4}{(2 - \tilde{g}_{DP})^2}. \tag{7}$$

The amplification enhancement for identical bandwidth is plotted in Fig. 2(a), together with the relation between the pumps at the DP and EP to achieve identical bandwidths

(inset). In Fig. 2(a), the critical point at which $\eta_G = 1$ (for an identical bandwidth) is denoted by p. Above point p (where $\tilde{g}_{DP} = 2\sqrt{2}F^2 \approx 1.17$), we have $\eta_G > 1$, i.e., the EP-based amplifier outperforms the DP-based amplifier. Notably, the value of the amplification-enhancement factor increases rapidly as the two amplifiers approach the lasing condition at $\tilde{g}_{DP} = \tilde{g}_{EP} = 2$.
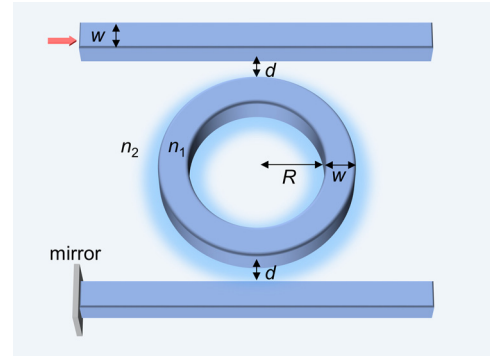

FIG. 3. A schematic diagram of the proposed photonic structure used in our FDTD simulations. The geometric and material parameters used in the simulations are as follows: waveguide width $w = 0.25$ μm (for both the straight and the ring waveguides), ring radius $R = 5$ μm, and edge-to-edge distances between the ring and waveguides $d = 0.15$ μm. To implement the mirror, we assume a thin layer of silver with a thickness of 100 nm. (In practice, there are several design principles for building a mirror; for instance, by using photonic crystals [23–25] or a section of different material [26].) The material refractive index is $n_1 = 3.47$ [corresponding to semiconductor materials such as silicon or (Al,Ga)As] and the background index is taken to be $n_2 = 1.44$. These values have been used before in DP-based microring amplifiers [4,27]. Finally, we model the applied gain by considering a gain curve with a finite bandwidth (for more details, see Appendix A).
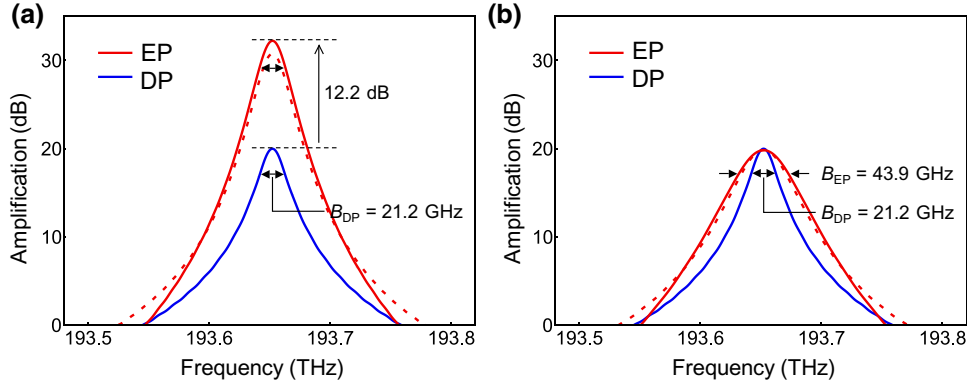
FIG. 4. Full-wave FDTD simulations for EP- and DP-based amplifiers operating close to $\lambda = 1.55$ μm and having (a) identical bandwidth and (b) identical maximum amplification, respectively. The solid and dashed red lines correspond to outputs at ports s_5 and s_4, respectively, while in the DP case (blue line) the output port is s_3. The superior performance in terms of higher amplification in (a) and larger bandwidth in (b) is evident in both cases. The operating points of both scenarios correspond to the square dots in Figs. 2(a) and 2(b), respectively. Excellent agreement between the FDTD results and the TCMT is observed in both cases. The details of the design parameters used in our simulations are listed in the caption of Fig. 3 and in the text.

Next, we consider the situation in which both amplifiers have the same maximum amplification ($G_{\mathrm{EP}} = G_{\mathrm{DP}}$) but different bandwidths. This condition is met at $\tilde{g}_{\mathrm{EP}} = 2 - \sqrt{2r(2 - \tilde{g}_{\mathrm{DP}})}$. In this case, the bandwidth enhancement factor η_B is given by following:

$$\eta_B \equiv \frac{B_{\mathrm{EP}}}{B_{\mathrm{DP}}}\Big|_{G_{\mathrm{EP}}=G_{\mathrm{DP}}} = \frac{\sqrt{2r}F}{\sqrt{2 - \tilde{g}_{\mathrm{DP}}}}. \qquad (8)$$

Figure 2(b) depicts η_B for increasing power amplification, together with the relation between the pumps at the DP and EP as a function of $\tilde{g}_{\mathrm{DP}}$. In Fig. 2(b), the critical point at which $\eta_B = 1$ (for an identical gain) is denoted by p. As before, the critical point p [identical to that of Fig. 2(a)] divides the operation domain into two regimes with $\eta_B < 1$ (dashed line) and $\eta_B > 1$ (solid line). We see that the value of η_B increases rapidly (eventually diverging) close to the lasing condition $\tilde{g}_{\mathrm{DP}} = \tilde{g}_{\mathrm{EP}} = 2$ (not shown in the figure).

Our discussion clearly demonstrates that operating at an EP can provide superior performance with very large values of η_G or η_B. However, from a practical perspective, the operating point should be chosen sufficiently far away from the lasing threshold to avoid noise-induced instabilities that can force the system into the lasing regime. Based on the detailed implementation and the noise level, this can pose an upper limit on the enhancement factors. In Fig. 2, we choose the mirror reflectivity as $r = 1$. This can be achieved, for example, by using photonic-crystal arrangements. Importantly, we note that if r deviates slightly from unity, the locations of the critical points p in Fig. 2(a) and 2(b) will shift, which will affect only the design parameters but not the general conclusion about the improved scaling of the gain-bandwidth product at an EP.

III. IMPLEMENTATION AND FULL-WAVE ANALYSIS

We have so far discussed the operation of our proposed EP-based OAs using optical TCMT. In order to confirm these predictions, we explore realistic implementations by performing two-dimensional (2D) full-wave FDTD simulations [28,29]. In particular, we study a 2D version of the schematic shown in Fig. 3 using the geometric and physical parameters listed in the caption of Fig. 3.

Figures 4(a) and 4(b) depict the simulation results for the two different scenarios discussed above, i.e., equal bandwidth or equal maximum amplification. The tuning of the amplifiers to operate in either of these regimes is done by setting up the correct gain parameters (for more details, see Appendix A). As shown in Fig. 4(a), for a fixed bandwidth of 21.2 GHz, a large amplification-enhancement factor is achieved with $\eta_G = 16.7$, corresponding to 12.2 dB. On the other hand, Fig. 4(b) shows that for an equal maximum amplification of 20 dB, the bandwidth in the EP case can be doubled, to $\eta_B = 2.1$. These results, which are obtained by using full-wave FDTD, are consistent with the theoretical values predicted by TCMT and clearly indicate the potential utility of the proposed structure.

Finally, Fig. 5 plots the field distribution for the two cases of DP and EP amplifiers (corresponding to the structure of Fig. 3 without and with the mirror) for the scenario depicted in Fig. 4(b) at resonance. In the EP case, one can observe the interference pattern that results due to the coexistence of CW and CCW waves. Note that the minimum of the field (see the inset) is not zero, which can be understood by recalling that the CCW component has a larger amplitude (due to amplification) than the CW component. This can also be confirmed by inspecting the time evolution of the fields (not shown here).
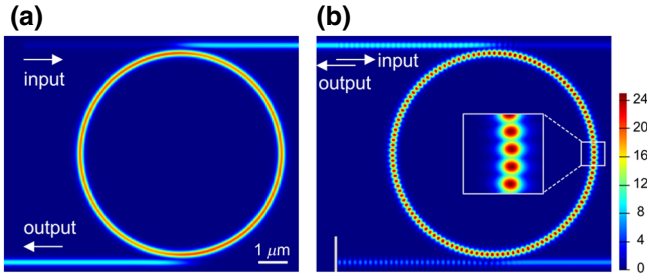
FIG. 5. The absolute value of the complex electric field distributions associated with (a) a DP-based and (b) and an EP-based amplifier for the resonant frequency when they both have an equal gain [i.e., corresponding to the case of Fig. 4(b)]. The inset in (b) highlights the interference pattern between the CW and CCW components in the latter case. The legend colors represent the value of the electric field normalized by the value of the input field. Note that the plotted fields correspond to the steady-state solution under external excitations and not to the eigenmodes of the system.

IV. DISCUSSION

The scaling features of the gain-bandwidth products associated with the geometry shown in Fig. 1 can be understood intuitively by noting that light traverses the ring twice in the forward and backward directions, which explains the gain enhancement. This observation raises the question of whether one can achieve the same performance by concatenating two ring resonators. As we discuss in Appendix B, this is indeed possible and gives exactly the same results. Interestingly, even in this latter case, one can show that the system exhibits a second-order EP, though an unusual one (for a detailed discussion, see Appendix B). This provides an advantage in terms of scalability, since one can add more microrings to obtain higher-order poles with far more superior performance. However, from a practical perspective, this latter design (with concatenated rings) will be more prone to fabrication errors (all the different ring parameters have to exactly match) and will require a more complex pumping scheme. This is in contrast to the design of Fig. 1, which is more robust and does not suffer from these problems (for a more detailed discussion of the robustness associated with the structure of Fig. 1, see Ref. [18]).

Another possible implementation that can combine the enhanced performance with the robustness is the S-bend ring resonator, which is also known to provide unidirectional coupling [30–32]. As shown in Appendix C, the output power demonstrates similar scaling behavior to that of EP-based OAs with a mirror.

Finally, we remark that in our current design of Fig. 1, the output is collected from the same input port. This may seem to pose some challenges. However, we note that, in general, almost all optical systems that involve lasers and amplifiers also contain additional nonreciprocal elements

such as isolators to protect the laser from any feedback. In our proposed structure, one can use a nonreciprocal three-port device, known as an optical circulator, to direct the output power from port s_5 to a different port than the input. Alternatively, one can also use port s_4 (as indicated in Fig. 1) as an output port. In this case, the expression for the gain-bandwidth product is more complex and less transparent but for large amplification, the output at s_4 will approximate to the output at s_5 and the improved scaling still holds. These predictions are confirmed using FDTD as indicated by the dashed red lines in Fig. 4. In producing these curves, the material gain is adjusted to satisfy the identical bandwidth and/or amplification conditions in both (a) and (b) as has been done before when the output port was s_5.

V. CONCLUSION

In conclusion, we introduce a design paradigm for optical amplifiers based on chiral exceptional points. An important feature of the proposed structure is the unique scaling of its gain-bandwidth product, which is different from that of conventional amplifiers and allows for achieving more gain or larger bandwidth. Mathematically, these results can be understood by noting that operating at an EP results in a double pole in the scattering coefficients (as opposed to a single pole in the standard DP case), i.e., s_{51} in Eq. (5) is proportional to s_{31}^2 in Eq. (1), which is the reason for the improved scaling for the gain-bandwidth product. Importantly, we have explored realistic implementations using current photonics technology to implement these amplifiers based on chiral exceptional points (for completeness, we have also confirmed these conclusions for a parity-time-($\mathcal{PT}$) based EP in Appendix D). Our results open the door for building a new generation of on-chip optical amplifiers with superior performance, which can prove beneficial for both classical and quantum optics applications. We emphasize that our proposed scheme can be directly mapped into other physical systems such as microwaves and acoustics. Finally, it would be interesting to explore the relation between the gain-bandwidth scaling of optical amplifiers operating at exceptional points as presented in our work and the linewidth enhancement predicted when the system operates as a laser [33,34]. We will pursue this in future work.

APPENDIX A: FDTD SIMULATION

The transmission of the passive resonators used in our simulations based on a DP or an EP without any material gain is shown in Fig. 6. The operating resonant frequency is located at $f_0 = 193.652$ THz, with a free spectral range (FSR) of 2.58 THz. The maximum transmission for the DP-based resonator is 0.998, indicating $\alpha/\gamma = 0.002$, which is a small quantity. The maximum transmission for the EP-based resonator is 0.952, which can be used to deduce the value of the reflection coefficient $r^2 = 0.954$—consistent with the $r^2 = 0.953$ obtained from a direct FDTD simulation test on the reflectivity of the mirror.

In our simulations, the applied material gain has a finite bandwidth as expressed by the Lorentz model:

$$\varepsilon(\omega) = \varepsilon_b + \frac{\varepsilon'\omega_0^2}{\omega_0^2 - \omega^2 - 2i\delta\omega}, \qquad (A1)$$

where ε_b is the permittivity of background material in the absence of any gain and/or loss or dispersion, ω_0 is the operating resonant frequency of the microring. $\delta = 10^{13}$ rad/s is the gain-curve linewidth, and ε' is a constant. The function $\varepsilon(\omega)$ is chosen to ensure that the gain curves are centered around the longitudinal mode of interest but have a bandwidth smaller than the free spectral range of the resonator in order to filter the undesired modes. To proceed with the computations, we set the value of ε' for every case and use FDTD to calculate the maximum amplification at resonance. This quantity can be then used to obtain the normalized gain values $\tilde{g}_{DP}$ and $\tilde{g}_{EP}$ (see the formulas for G_{DP} and G_{EP}), which in turn allows us to compare our FDTD results with the results obtained using Eqs. (6)

and (7) in the main text. In particular, in the simulations of Fig. 3 in the main text, we use $\varepsilon' = -2.133 \times 10^{-4}$ for the DP amplifier and $\varepsilon' = -2.00194 \times 10^{-4}$ and $\varepsilon' = -1.6198 \times 10^{-4}$ for the EP amplifiers of Figs. 3(a) and 3(b), respectively.

APPENDIX B: CASCADED AMPLIFIERS AND EXCEPTIONAL POINTS

In the EP-based amplifier proposed in Fig. 1, light travels from port s_1 to s_3, gets reflected, and travels back to the same input port in the opposite direction. This intuitive picture can explain the enhancement in the net amplification. It also raises the question of whether it is possible to achieve the same functionality by concatenating two ring resonators. By referring to Fig. 7(a), it is not difficult to see that this structure has an identical scattering coefficient to that of Fig. 1 with $r\exp(i\phi) = 1$. This is also confirmed by using FDTD with $\varepsilon' = -2.00194 \times 10^{-4}$, as shown in Fig. 7(b).

At first sight, this may seem surprising but, interestingly, the system in Fig. 7 also has a chiral EP, since mode a_{cw} couples to b_{ccw}, while the opposite is not true. In fact, here there is also another chiral EP arising from the unidirectional coupling from b_{cw} to a_{ccw}, which would allow the amplifier to work for backward-propagating light as well. Interestingly, this scheme can be used to build amplifiers with higher-order EPs by just cascading as many rings as needed, thus providing a clear advantage in terms of scalability. In practice, however, this system will be more prone
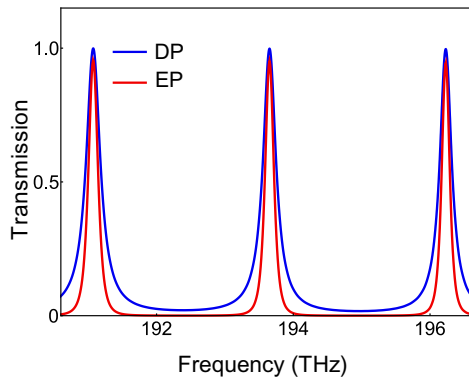

FIG. 6.   The transmission of the DP- and EP-based resonators without any material gain. In the amplifiers discussed in the text, we introduce a material gain, based on the Lorentz model, to the microring resonator.
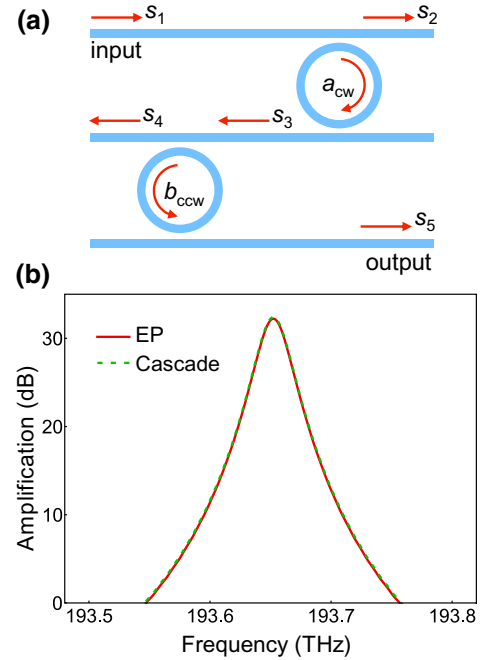

FIG. 7.   (a) A cascaded amplifier can achieve the same functionality as the structure in Fig. 1 with $r\exp(i\phi) = 1$, as confirmed in (b) using FDTD.

to fabrication errors, since it will require all the rings to have identical parameters within a small margin of error (disorder in the coupling parameters will not affect the chiral EP). Additionally, it will also require a complex pumping scheme and more power consumption to provide gain to all the rings. On the other hand, the structure proposed in Fig. 1 does not suffer from these problems. In particular, any variation in the ring parameter will affect both modes equally, which will shift the central frequency but retain the same gain-bandwidth relation. Additionally, it contains only one ring and thus requires simpler pumping and less power consumption.

APPENDIX C: S-BEND RING RESONATOR

Another possible implementation that can combine the enhanced performance with the robustness is the S-bend ring resonator shown in Fig. 8. This structure is also known to provide unidirectional coupling [30–32]. By using the scattering matrices $S_j = \begin{bmatrix} t_j & i\kappa_j \\ i\kappa_j & t_j \end{bmatrix}$ (with $t_j^2 + \kappa_j^2 = 1$, where $j = 1, 2, 3, 4$) at each junction (denoted by the dashed black lines in Fig. 8), we obtain the relation between the electric field amplitudes a_{cw} and a_{ccw} at the beginning and at the end of each section along the ring between any two junctions. This, in turn, can be used to calculate the scattering coefficients. In particular, when $S_2 = S_4$ and $S_3 = I$, where I is the unit matrix (i.e., we remove the lower waveguide altogether), we obtain the following:

$$u_{51} \equiv \frac{u_5}{u_1} = \frac{2\Gamma t_2 \kappa_1^2 \kappa_2^2 \exp(i\omega\tau)}{[1 - \Gamma t_1 t_2^2 \exp(i\omega\tau)]^2}, \quad \text{(C1)}$$

where $\Gamma = \exp[-2\pi \, \mathrm{Im}(n_{eff})L/\lambda]$ is the round-trip gain of the ring resonator and $\tau = \mathrm{Re}(n_{eff})L/c$. Here, n_{eff} is the effective index of the ring-waveguide mode, L is the circumference of the ring waveguide, and λ is the free-space wavelength. The maximum amplification (at the resonant frequency) and the bandwidth are then found to be as follows:

$$G_S = \frac{4\Gamma^2 t_2^2 \kappa_1^4 \kappa_2^4}{(1 - \Gamma t_1 t_2^2)^4},$$
$$B_S = 2F \frac{1 - \Gamma t_1 t_2^2}{\sqrt{\Gamma t_1 t_2}} \tau^{-1}. \quad \text{(C2)}$$

Consequently, the gain-bandwidth product is given by following:

$$\chi_S \equiv G_S^{1/4} B_S = 2\sqrt{2} F \kappa_1 \kappa_2 (t_1 t_2)^{-1/2} \tau^{-1}, \quad \text{(C3)}$$

with the right-hand side being a constant. This last expression reveals that the gain-bandwidth product in the S-bend geometry scales in a similar fashion to the structure shown in Fig. 1. From an experimental perspective, one can add
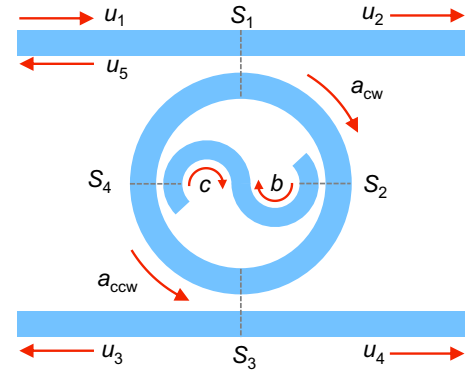

FIG. 8. The S-bend ring can provide a unidirectional coupling between the CW and CCW modes. This structure is studied with scattering matrices S_j ($j = 1, 2, 3, 4$) in the four coupling regions (dashed lines).

the second waveguide and measure the output from u_4, where it can be shown that the output power demonstrates similar scaling behavior.

APPENDIX D: AMPLIFIERS AT EPs IN $\mathcal{PT}$ SYMMETRIC DIMERS

In order to make the connection between our results here and the work on $\mathcal{PT}$ symmetry—and, at the same time, illustrate that the predicted superior performance of EP-based amplifiers is general and not restricted to the geometry investigated in the main text—we consider an amplifier based on the archetypal $\mathcal{PT}$-symmetric dimer [13,14,35–41] shown in Fig. 9(a). It consists of two identical microrings coupled to each other with coupling rate κ. Both rings have the same radiation loss and are coupled to identical waveguides with equal coupling coefficients. Additionally, we assume that the top ring has a material gain g while the lower ring has an additional loss factor $-g$. By using TCMT, we obtain the following:

$$\frac{da_{cw}}{dt} = [i(\omega_0 - \omega) - \gamma - \alpha + g]a_{cw} + i\kappa b_{ccw} + \sqrt{2\gamma}s_1,$$
$$\frac{db_{ccw}}{dt} = [i(\omega_0 - \omega) - \gamma - \alpha - g]b_{ccw} + i\kappa a_{cw},$$
$$s_3 = -\sqrt{2\gamma}b_{ccw}. \quad \text{(D1)}$$

By solving the above system, we obtain the expression for the steady state transfer function as follows:

$$s_{31} \equiv \frac{s_3}{s_1} = \frac{-2i\kappa\gamma}{[i(\omega - \omega_0) + \gamma + \alpha]^2 + \kappa^2 - g^2}. \quad \text{(D2)}$$

Note that this solution is only valid below the lasing threshold $g^2 = \kappa^2 + (\gamma + \alpha)^2$. The system exhibits an EP when $g = \kappa$. Under this condition, the maximum
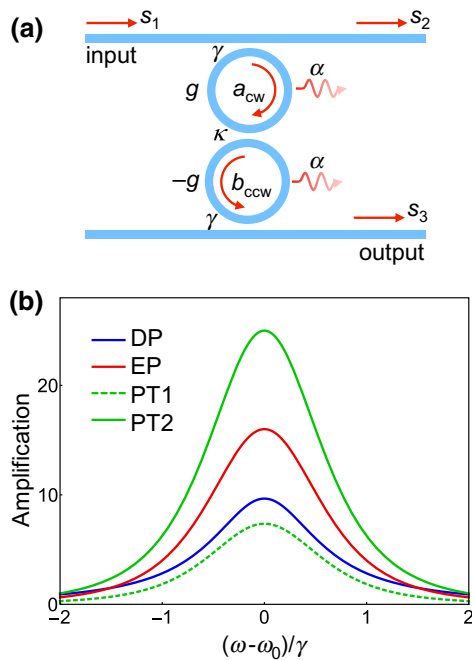
FIG. 9. (a) A $\mathcal{PT}$-dimer-based optical amplifier having an exceptional point at $g = \kappa$. (b) A comparison between the structure in (a) and those in Fig. 1 (with and without a mirror) for identical γ and assuming $\alpha = 0$, when $g_{\mathrm{PT1}} = 1.36\gamma$ (dashed green line) and $g_{\mathrm{PT2}} = 2.5\gamma$ (solid green line). Clearly, one can increase the amplification of the $\mathcal{PT}$ amplifier while at the same time maintaining the same bandwidth. From a practical perspective, however, increasing the amplification requires stronger coupling κ (i.e., smaller separation between the two rings), which is limited by the fabrication tolerance.

amplification is given by $G_{\mathrm{PT}} = 4g^2\gamma^2/(\gamma + \alpha)^4$, while the bandwidth takes the value $B_{\mathrm{PT}} = 2F(\gamma + \alpha)$. Interestingly, in contrast to the structure investigated in the main text, here the bandwidth is independent of the gain. In other words, the gain-bandwidth product can be made arbitrarily large by a judicious choice of the design parameters and the applied gain—a feature that has previously been noted for linear microwave amplifiers based on wave-mixing processes [6,42], though without establishing the connection with the physics of exceptional points. To illustrate this point, Fig. 9(b) depicts a comparison between the three different structures of Fig. 1 (with and without a mirror) and Fig. 9(a). Here, we choose $\alpha \approx 0$ and identical values of γ for all three devices. The bandwidth of the $\mathcal{PT}$-based amplifier is $2F\gamma \approx 1.28\gamma$. This same bandwidth can be achieved for the other two geometries by setting $g_{\mathrm{DP}} = (2 - F)\gamma \approx 1.36\gamma$ and $g_{\mathrm{EP}} = \gamma$. When $g_{\mathrm{PT}} = g_{\mathrm{DP}}$, the $\mathcal{PT}$ system exhibits lower amplification, as shown by the dashed green line in Fig. 9(b). However, in theory, the maximum amplification can be increased indefinitely by increasing g_{PT} without affecting the bandwidth. For example, by choosing $g_{\mathrm{PT}} = 2.5\gamma$, the maximum amplification of the $\mathcal{PT}$ structure can significantly

surpass that of the other two scenarios, while at the same time maintaining the same bandwidth [the solid green line in Fig. 9(b)].

From a practical perspective, however, increasing the gain-bandwidth product will require the fabrication of samples with stronger coupling between the two rings, which is obviously limited by the minimum achievable edge-to-edge separation between the rings. Additionally, the $\mathcal{PT}$ geometry is very sensitive to fabrication errors and tolerance, as well as uncertainties in the operating conditions such as, for instance, thermal effects.

[1] N. K. Dutta and Q. Wang, *Semiconductor Optical Amplifiers* (World Scientific, Singapore, 2013), 2nd ed.

[2] M. J. Connelly, *Semiconductor Optical Amplifiers* (Kluwer Academic, Boston, 2002).

[3] K. Hattori, T. Kitagawa, M. Oguma, Y. Ohmori, and M. Horiguchi, Erbium-doped silica-based waveguide amplifier integrated with a 980/1530 nm WDM coupler, Electron. Lett. **30**, 856 (1994).

[4] K. Amarnath, R. Grover, S. Kanakaraju, and P.-T. Ho, Electrically pumped InGaAsP-InP microring optical amplifiers and lasers with surface passivation, IEEE Photonics Technol. Lett. **17**, 2280 (2005).

[5] A. A. Clerk, M. H. Devoret, S. M. Girvin, F. Marquardt, and R. J. Schoelkopf, Introduction to quantum noise, measurement, and amplification, Rev. Mod. Phys. **82**, 1155 (2010).

[6] A. Metelmann and A. A. Clerk, Quantum-Limited Amplification via Reservoir Engineering, Phys. Rev. Lett. **112**, 133904 (2014).

[7] A. Metelmann and A. A. Clerk, Nonreciprocal Photon Transmission and Amplification via Reservoir Engineering, Phys. Rev. X **5**, 021025 (2015).

[8] A. Metelmann and A. A. Clerk, Nonreciprocal quantum interactions and devices via autonomous feed forward, Phys. Rev. A **95**, 013837 (2017).

[9] C. F. Ockeloen-Korppi, E. Damskägg, J. M. Pirkkalainen, T. T. Heikkilä, F. Massel, and M. A. Sillanpää, Low-Noise Amplification and Frequency Conversion with a Multi-port Microwave Optomechanical Device, Phys. Rev. X **6**, 041024 (2016).

[10] T. Chien, O. Lanes, C. Liu, X. Cao, P. Lu, S. Motz, G. Liu, D. Pekker, and M. Hatridge, Multiparametric amplification and qubit measurement with a Kerr-free Josephson ring modulator, arXiv:1903.02102.

[11] W. D. Heiss, Exceptional points of non-Hermitian operators, J. Phys. A **37**, 2455 (2004).

[12] M. Müller and I. Rotter, Exceptional points in open quantum systems, J. Phys. A **41**, 244018 (2008).

[13] R. El-Ganainy, K. G. Makris, M. Khajavikhan, Z. H. Musslimani, S. Rotter, and D. N. Christodoulides, Non-Hermitian physics and PT symmetry, Nat. Phys. **14**, 11 (2018).

[14] L. Feng, R. El-Ganainy, and L. Ge, Non-Hermitian photonics based on parity-time symmetry, Nat. Photon. **11**, 752 (2017).

[15] S. K. Özdemir, S. Rotter, F. Nori, and L. Yang, Parity-time symmetry and exceptional points in photonics, Nat. Mat. **18**, 783 (2019).

[16] K. Vahala, *Optical Microcavities* (World Scientific, Singapore, 2004).

[17] S. Fan, W. Suh, and J. D. Joannopoulos, Temporal coupled-mode theory for the Fano resonance in optical resonators, J. Opt. Soc. Am. A **20**, 569 (2003).

[18] Q. Zhong, J. Ren, M. Khajavikhan, D. N. Christodoulides, S. K. Özdemir, and R. El-Ganainy, Sensing with Exceptional Surfaces in Order to Combine Sensitivity with Robustness, Phys. Rev. Lett. **122**, 153902 (2019).

[19] J. Wiersig, Enhancing the Sensitivity of Frequency and Energy Splitting Detection by Using Exceptional Points:Application to Microcavity Sensors for Single-Particle Detection, Phys. Rev. Lett. **112**, 203901 (2014).

[20] J. Wiersig, Sensors operating at exceptional points: General theory, Phys. Rev. A **93**, 033809 (2016).

[21] B. Peng, S. K. Özdemir, M. Liertzer, W. Chen, H. Yilmaz, J. Wiersig, S. Rotter, and L. Yang, Chiral modes and directional emission at exceptional points, Proc. Natl. Acad. Sci. USA (PNAS) **113**, 6845 (2016).

[22] J. Wiersig, in *Parity-time Symmetry and its Applications*, edited by D. Christodoulides and J. Yang (Springer Singapore, Singapore, 2018), pp. 155–184.

[23] P. B. Deotare, M. W. McCutcheon, I. W. Frank, M. Khan, and M. Loncar, High quality factor photonic crystal nanobeam cavities, Appl. Phys. Lett. **94**, 121106 (2009).

[24] Q. Quan, P. B. Deotare, and M. Loncar, Photonic crystal nanobeam cavity strongly coupled to the feeding waveguide, Appl. Phys. Lett. **96**, 203102 (2010).

[25] B. J. M. Hausmann, B. J. Shields, Q. Quan, Y. Chu, N. P. de Leon, R. Evans, M. J. Burek, A. S. Zibrov, M. Markham, D. J. Twitchen, H. Park, M. D. Lukin, and M. Loncar, Coupling of NV centers to photonic crystal nanobeams in diamond, Nano Lett. **13**, 5791 (2013).

[26] S. Zamek, L. Feng, M. Khajavikhan, D. T. H. Tan, M. Ayache, and Y. Fainman, Micro-resonator with metallic mirrors coupled to a bus waveguide, Opt. Express **19**, 2417 (2011).

[27] K. Amarnath, Active microring and microdisk optical resonators on indium phosphide. Thesis, University of Maryland, 2006.

[28] A. Taflove and S. C. Hagness, *Computational Electrodynamics: The Finite-Difference Time-Domain Method* (Artech House, Boston, London, 2005), 3rd ed.

[29] A. Z. Elsherbeni and V. Demir, *The Finite-Difference Time-Domain Method for Electromagnetics with* MATLAB *Simu-lations (Electromagnetics and Radar)* (Scitech Publishing, Raleigh, North Carolina, 2015), 2nd ed.

[30] J. P. Hohimer, G. A. Vawter, and D. C. Craft, Unidirectional operation in a semiconductor ring diode laser, Appl. Phys. Lett. **62**, 1185 (1993).

[31] S. Kharitonov and C.-S. Bres, Isolator-free unidirectional thulium-doped fiber laser, Light Sci. Appl. **4**, e340 (2015).

[32] J. Ren, Y. G. N. Liu, M. Parto, W. E. Hayenga, M. P. Hokmabadi, D. N. Christodoulides, and M. Khajavikhan, Unidirectional light emission in PT-symmetric microring lasers, Opt. Express **26**, 27153 (2018).

[33] G. Yoo, H.-S. Sim, and H. Schomerus, Quantum noise and mode nonorthogonality in non-Hermitian *PT*-symmetric optical resonators, Phys. Rev. A **84**, 063833 (2011).

[34] J. Zhang, B. Peng, S. K. Özdemir, K. Pichler, D. O. Krimer, G. Zhao, F. Nori, Y.-X. Liu, S. Rotter, and L. Yang, A phonon laser operating at an exceptional point, Nat. Photon. **12**, 479 (2018).

[35] R. El-Ganainy, K. G. Makris, D. N. Christodoulides, and Z. H. Musslimani, Theory of coupled optical PT-symmetric structures, Opt. Lett. **32**, 2632 (2007).

[36] A. Guo, G. J. Salamo, D. Duchesne, R. Morandotti, M. Volatier-Ravat, V. Aimez, G. A. Siviloglou, and D. N. Christodoulides, Observation of PT-Symmetry Breaking in Complex Optical Potentials, Phys. Rev. Lett. **103**, 093902 (2009).

[37] C. E. Rüter, K. G. Makris, R. El-Ganainy, D. N. Christodoulides, M. Segev, and D. Kip, Observation of parity-time symmetry in optics, Nat. Phys. **6**, 192 (2010).

[38] H. Hodaei, M.-A. Miri, M. Heinrich, D. N. Christodoulides, and M. Khajavikhan, Parity-time-symmetric microring lasers, Science **346**, 975 (2014).

[39] B. Peng, S. K. Özdemir, F. Lei, F. Monifi, M. Gianfreda, G. L. Long, S. Fan, F. Nori, C. M. Bender, and L. Yang, Parity-time-symmetric whispering-gallery microcavities, Nat. Phys. **10**, 394 (2014).

[40] L. Chang, X. Jiang, S. Hua, C. Yang, J. Wen, L. Jiang, G. Li, G. Wang, and M. Xiao, Parity-time symmetry and variable optical isolation inactive-passive-coupled microresonators, Nat. Photon. **8**, 524 (2014).

[41] J. Schindler, A. Li, M. C. Zheng, F. M. Ellis, and T. Kottos, Experimental study of active *LRC* circuits with $\mathcal{PT}$ symmetries, Phys. Rev. A **84**, 040101(R) (2011).

[42] T. Roy, S. Kundu, M. Chand, A. M. Vadiraj, A. Ranadive, N. Nehra, M. P. Patankar, J. Aumentado, A. A. Clerk, and R. Vijay, Broadband parametric amplification with impedance engineering: Beyond the gain-bandwidth product, Appl. Phys. Lett. **107**, 262601 (2015).